Research article

Numerical investigation of quantitative pulmonary pressure ratio in different degrees of stenosis

Fan He[1],*, Minru Li[1], Xinyu Wang[1], Lu Hua[2] and Tingting Guo[2]

[1] School of Science, Beijing University of Civil Engineering and Architecture, Beijing 100044, China
[2] Thrombosis Center, National Clinical Research Center for Cardiovascular Diseases, State Key Laboratory of Cardiovascular Disease, Fuwai Hospital, National Center for Cardiovascular Diseases, Chinese Academy of Medical Sciences and Peking Union Medical College, Beijing 100037, China

* **Correspondence:** Email: hefan@bucea.edu.cn.

Abstract: *Background*: Pulmonary artery stenosis endangers people's health. Quantitative pulmonary pressure ratio (QPPR) is very important for clinicians to quickly diagnose diseases and develop treatment plans. *Objective*: Our purpose of this paper is to investigate the effects of different degrees (50% and 80%) of pulmonary artery stenosis on QPPR. *Methods*: An idealized model is established based on the normal size of human pulmonary artery. The hemodynamic governing equations are solved using fluid-structure interaction. *Results*: The results show that the QPPR decreases with the increase of stenosis degree, and it is closely related to the pressure drop at both ends of stenosis. Blood flow velocity and wall shear stress are sensitive to the stenosis degree. When the degree of stenosis is 80%, the amplitude of changes of blood flow velocity and wall shear stress at both ends of stenosis is lower. *Conclusions*: The results suggest that the degree of pulmonary artery stenosis has a significant impact on QPPR and hemodynamic changes. This study lays a theoretical foundation for further study of QPPR.

Keywords: stenosis; pulmonary artery; hemodynamics; numerical simulation; fluid-structure interaction

1. Introduction

Pulmonary artery stenosis may be caused by a variety of conditions, such as autoimmune diseases, that lead to stenosis or occlusion due to vasculitis of large arteries and branch arteries and stenosis of

adventitia diameter of vascular wall itself or tumor formation, etc. [1]. Understanding the mechanical properties of the physiological structure and blood flow of pulmonary artery stenosis is of great significance for the guidance of clinical diagnosis and treatment. It is well known that fractional flow reserve (FFR) measurement has been widely used clinically in coronary artery diseases. It can be used as an effective supplement to determine whether coronary artery stenosis will cause myocardial ischemia and other symptoms, and to evaluate the blood supply function of the vessels [2,3]. However, FFR is invasive. Particularly, the use of pressure wire and contrast agent is not conducive to patients with low physical fitness. The clinical procedure takes a long time, which is risky and expensive. Mock circulatory loops are very useful to test *ex vivo* arteries by mimicking physiological pulsatile blood pressure and flow. With respect to *in-vivo* experiments, which are invasive, they offer the advantage of the simultaneous, accurate and direct measurement of the flow parameters and deformation of the arterial wall [4]. Quantitative flow ratio (QFR), as a new technology for rapid calculation of FFR, is gradually applied to clinical diagnosis and treatment. According to the three-dimensional model of coronary artery, the ratio of distal stenosis pressure to proximal stenosis pressure is calculated noninvasively using numerical simulation [5,6]. QFR does not need to use guide wire and vasodilator, and has the advantages of short calculation time. In addition, in clinical practice, QFR could be used for patients who are allergic to vasodilators and cannot undergo invasive FFR measurement and its effect is superior to FFR. At present, the clinical diagnosis of pulmonary hypertension and other diseases depends mainly on the insertion of pressure guide wire from femoral vein/carotid artery and multiple perfusions of contrast agent to capture physiological information such as stenosis location, degree and morphology [7]. Therefore, more researchers are committed to applying the diagnosis and treatment methods of coronary artery diseases to pulmonary artery diseases, building a three-dimensional model of pulmonary artery, non-invasive diagnosis and treatment, improving the cure rate of pulmonary vascular disease and achieving better clinical results in the treatment of pulmonary artery stenosis. Previous studies established pulmonary artery models through numerical simulation to study hemodynamic changes. These results are consistent with physiological facts, which confirms the feasibility of the modeling study in vitro [8,9]. They show that the geometric configuration, degree and length of stenosis affect coronary hemodynamics and FFR [10–12].

At present, great progress has been made in numerical simulation of pulmonary hemodynamics. The hemodynamic characteristics of pulmonary circulation could be accurately simulated by computational fluid dynamics [13]. In the study of pulmonary artery stenosis, the distributions of blood flow velocity, pressure and wall shear stress are investigated, which play important roles in judging the condition of different degrees of stenosis [14]. However, few studies have focused on the numerical modeling of FFR in pulmonary artery stenosis. In this paper, FFR in pulmonary artery is denoted by quantitative pulmonary pressure ratio (QPPR), which is very important for clinicians to quickly diagnose diseases and develop treatment plans. The purpose of this paper is to explore the influences of stenosis degree on pulmonary artery hemodynamics and QPPR.

2. Numerical methods

2.1. Geometric model

The pulmonary artery is divided into left pulmonary artery (LPA), right pulmonary artery (RPA) and their branches. The model used in this paper includes left and right pulmonary arteries, left truncus anterior (LTA) and right truncus anterior (RTA). Figure 1 shows the model geometry. It is an idealized

model based on the range of the physiological size of normal human pulmonary artery [15]. The inner diameter of the anterior trunk of the left lung apex is reduced to different degrees, and then the models with different degrees of stenosis are obtained. The formula of stenosis severity could be calculated as the follows [16]:

$$S_0 = \frac{R_0 - R_{min}}{R_0} \times 100 \tag{1}$$

where, S_0 indicates stenosis severity, R_0 represents the radius of the uniform part of the pipe, R_{min} represents the minimum radius of the narrow area of the pipe. This paper mainly focuses on the changes of pulmonary artery hemodynamics under 50% and 80% stenosis severity. The lower right corner of Figure 1 is the inlet velocity diagram during three cycles, and the boundary conditions at the outlets are constant pressures.
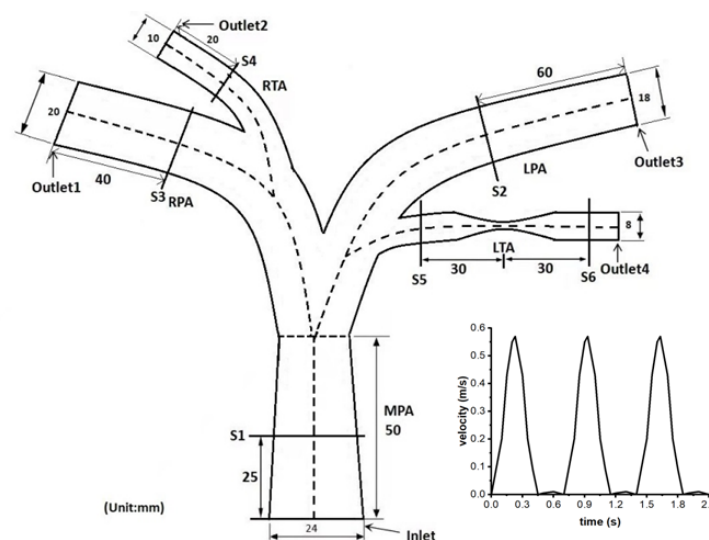

Figure 1. The model geometry.

In this study, six sections S1–S6 are selected, and then their hemodynamic changes are analyzed. Section S1 is 25 mm away from the inlet, sections S2, S3 and S4 are 60, 40 and 20 mm away from each outlet and sections S5 and S6 are 30 mm away from the narrow center. The transient pressures of the distal and proximal to the stenosis are required when calculating QPPR. The proximal pressure is taken from the entrance to the trunk of a pulmonary artery model and the distal pressure is taken from the exit with the stenotic trunk. The calculation formula of QPPR is defined.

$$QPPR = \frac{P_d}{P_a} \tag{2}$$

where, P_d is the maximum systolic pressure at the distal end of the diseased vessel, P_a represents the maximum systolic pressure of the proximal end of the diseased vessel.

The relationship between P_d and P_a could be expressed.

$$\Delta P = fV + sV^2 \tag{3}$$

where $\triangle P$ is the pressure loss, f is the coefficient of pressure loss due to viscous friction, V is flow

velocity and s is the coefficient of pressure loss due to flow separation or localized turbulence downstream from the stenosis. The detailed explanation of Eq (3) can be found in Gould's work [17].

2.2. Material properties

It is assumed that the vascular wall is a linear elastic and isotropic material. The elastic modulus is $E = 2\,\text{Mpa}$ [18], Poisson's ratio is $v = 0.49$ [13] and solid density is $\rho_S = 1120\,\text{kg/m}^3$ [19]. Strictly speaking, blood is composed of a variety of tangible elements (such as red blood cells) and plasma. The influence of visible elements in blood on macro flow could be ignored, and blood is regarded as Newtonian fluid in large blood vessels [20]. Blood flow is set to be laminar, incompressible. Blood density is $\rho_f = 1060\,\text{kg/m}^3$ [21], and dynamic viscosity is $\mu = 0.004\,\text{Pa·s}$ [21].

2.3. Numerical model

In the calculation process, the coupling between fluid and solid is very important. In the same time step, the computational fluid dynamics equations and the computational solid governing equations are solved, respectively, and the solution convergence is achieved by exchanging the data of solid and fluid domains at the fluid-solid coupling interface. The blood flow governing equations are as follows [22].

$$\rho_f \left[\frac{\partial \mathbf{u}}{\partial t} + ((\mathbf{u} - \mathbf{u_m}) \cdot \nabla)\mathbf{u} \right] = -\nabla p_f + \mu \nabla^2 \mathbf{u} \tag{4}$$

$$\nabla \cdot \mathbf{u} = 0 \tag{5}$$

where $\mathbf{u}$ is blood flow velocity, $\mathbf{u_m}$ is grid velocity, p_f is blood flow pressure. The governing equations of vessel wall are:

$$\sigma_{ij} = \lambda \varepsilon_{ij} \delta_{ij} + 2G\varepsilon_{ij} \tag{6}$$

$$\varepsilon_{ij} = \frac{1}{2}(d_{i,j} + d_{j,i}) \tag{7}$$

$$\varepsilon_{ij} = \left(\frac{1+v}{E}\right)\sigma_{ij} - \frac{v}{E}\sigma_{kk}\delta_{ij} \tag{8}$$

where, λ, G are called lame elastic constants, σ_{ij} is the stress component, ε_{ij} is the strain component, δ_{ij} is kronecker delta, d_i and d_j represent the displacements in the i and j directions respectively and $\cdot,i$ and $\cdot,j$ represent the derivatives of the i and j variables, respectively.

The pressure and deformation data generated by fluid and solid domains are exchanged. When the fluid-solid coupling is carried out, the fluid velocity on the interface is the same as the solid velocity, and their moving displacements are also the same. The fluid surface force acts on the interface as the solid surface load, which could be expressed by the following mathematical expressions.

$$\mathbf{u} = \mathbf{U} \tag{9}$$

$$\mathbf{d_s} = \mathbf{d_f} \tag{10}$$

$$\boldsymbol{\sigma}_s \cdot \mathbf{n_s} = \boldsymbol{\sigma}_f \cdot \mathbf{n_f} \tag{11}$$

where $\mathbf{U}$ is the solid boundary velocity, $\mathbf{d}_s$ and $\mathbf{d}_f$ represent the displacements of solid and fluid respectively, $\boldsymbol{\sigma}_s$ and $\boldsymbol{\sigma}_f$ are solid and fluid stress tensors and $\mathbf{n}_s$ and $\mathbf{n}_f$ denote solid and fluid boundary normal unit vectors, respectively.

2.4. Grid division

In this paper, the established geometric models are imported into the transient structure and fluid analysis modules of the finite element software ANSYS to mesh the solid and fluid domains, respectively. When hexahedral mesh is selected for division, the results show that the mesh is highly distorted at the arterial bend and bifurcation, and the calculation is forced to terminate. Therefore, tetrahedral mesh is used. The grid numbers will affect the accuracy of results. Therefore, we analyze the sensitivity. The quantity is increased from about 20,000 to 120,000 for testing. Finally, the quantity in Table 1 is selected to guarantee the accuracy of calculation. The grid maps of two models are shown in Figure 2.

Table 1. Grid and node numbers of two models.

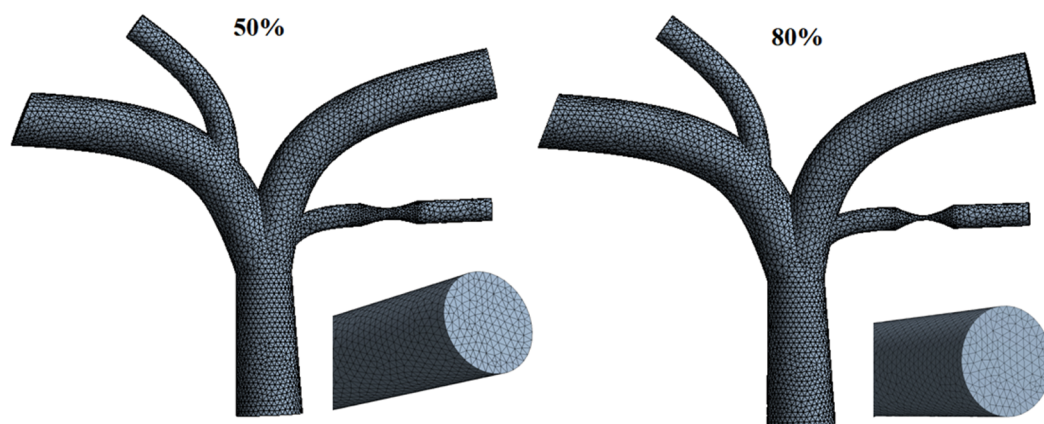| Stenosis degree	Fluid		Solid	
	Grid numbers	Node numbers	Grid numbers	Node numbers
50%	97,772	19,551	66,914	132,456
80%	96,324	19,254	65,644	130,084

Figure 2. Grid maps of two models.

2.5. Boundary conditions and solution settings

For the fluid, the inlet velocity is shown in Figure 3 [21]. The outlet conditions are set to be the constant pressure of 1000 Pa, and the fluid is set at the solid surface without slip and penetration conditions. For the vessel wall, the freedom degrees of the inlet and outlet end faces are set to be fixed, and the inner surface of the vessel wall is set as the fluid-wall interface. The solution time is set to 2.1 s. In this paper, the sensitivity of the time step is tested, and the time steps of 0.005 and 0.01 s are selected for calculation. There is no significant difference between the calculated results of 0.005 and 0.01 s time steps. The period is 0.7 s. For each time step, when the iteration error is less than 1×10^{-4}, the

solution is considered to be convergent. The system coupling module is used for two-way coupling solution, and the results of the third cycle are selected for the analysis. We apply an arbitrary Lagrangian-Eulerian (ALE) finite element method to simulate the flow field with moving structures. Finite element methods for solving partial differential equations use weighted residual concepts. The idea behind the finite element method is to break the spatial domain up into a number of simple geometric elements such as triangles or quadrilaterals. The weighted residual concept is then used to approximate the solution function over each finite element domain. Partial differential equations are therefore transformed into sets of ordinary differential equations in time.
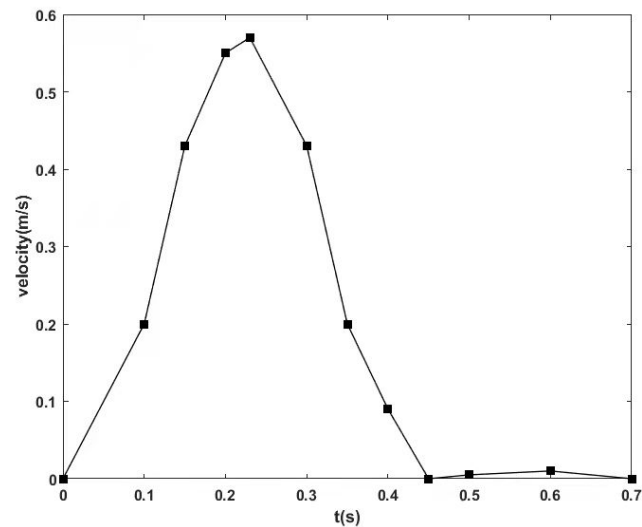

Figure 3. The inlet velocity.

3. Results

In this work, we perform numerical calculation of hemodynamics under 50% and 80% degrees of stenosis. Due to different degrees, grid numbers in the two models are different. Except for these, the experimental environment for modeling (such as boundary conditions, etc.) and other parameters are the same. Through numerical simulation, pressures at different sections could be obtained, including P_d and P_a in Eq (2). Thus, QPPR could be calculated accordingly, as shown in Table 2. It could be seen that the greater the degree of stenosis, the lower the QPPR.

Table 2. QPPR under different degrees of stenosis.

Stenosis degree	50%	80%
QPPR	0.8738	0.7281

When the degrees of stenosis are 50% and 80%, the pressure distributions at different sections are shown in Figure 4. The sensitivity of pressures at sections S1–S4 to the change of stenosis degree is low. The pressure range of section S1 is between 300 and 1800 Pa, and that of sections S2–S4 is between 800 and 1300 Pa. Overall, it could be seen that the pressure under 80% stenosis is slightly lower than that under 50% stenosis. The pressure change at both ends of the stenosis is very important

for the analysis of hemodynamic characteristics. The QPPR is also directly related to the pressure drop at both ends of the stenosis. It is obvious from Figure 4 that no matter the degree of stenosis is 50% or 80%, the pressure drop is high. During systole, the pressure at section S5 near the stenosis fluctuates greatly, and gradually tends to be stable in diastole. The pressure at section S6 at the distal end of the stenosis is close to the outlet pressure, especially when the degree of stenosis is 80%.

Four moments, namely 0.10, 0.23, 0.40 and 0.60 s, are selected, which represent pre-systolic, mid-systolic, pre-diastolic and late diastolic, respectively. Figure 5 shows the pressure contours at these four moments, which clearly present that there is the low pressure at the throat of the stenosis, and there is pressure drop at both ends of the stenosis. When the stenosis is 50%, the artery is in a high-pressure state in the late diastole. However, it is in a low-pressure state when the stenosis is 80%.
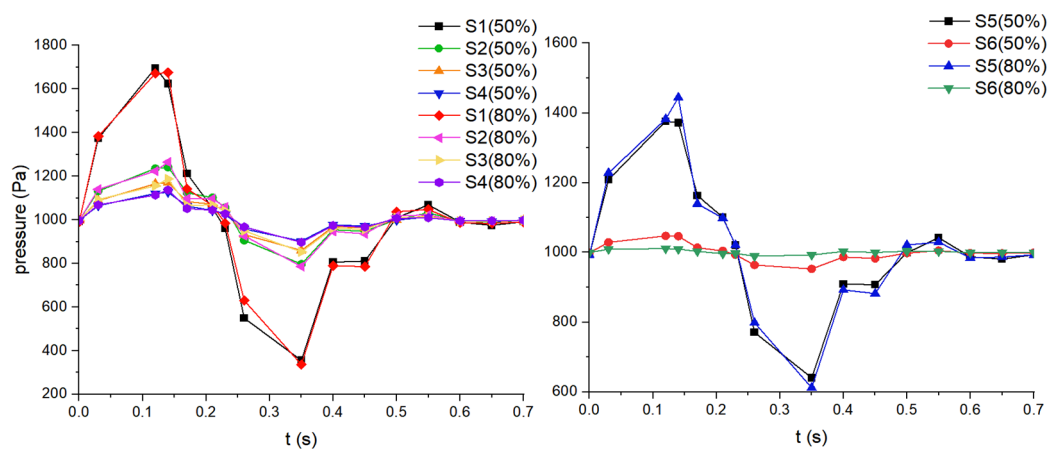

Figure 4. Pressure distributions at different sections in two models.
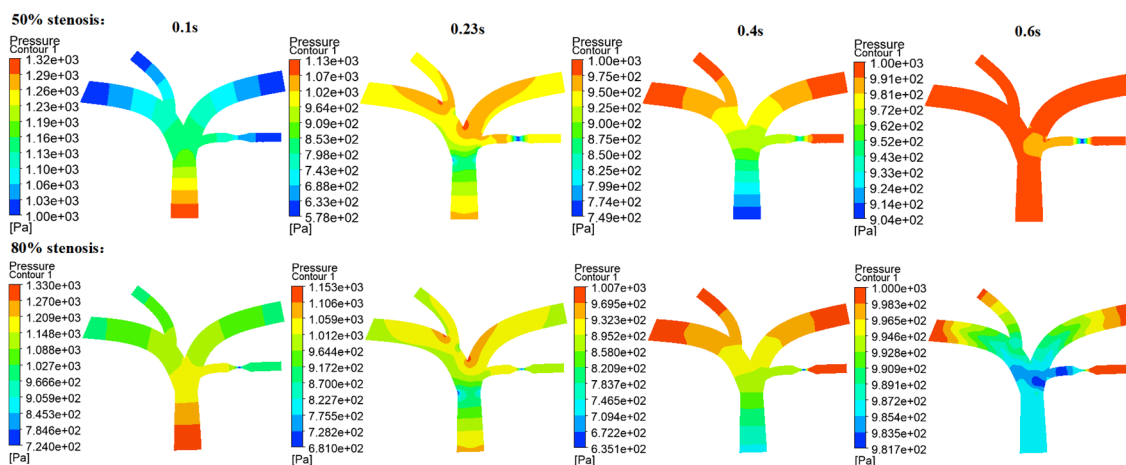

Figure 5. Pressure contours at different moments in two models.

Due to the interaction between the pressure and the wall deformation, it has a certain impact on the blood flow velocity. Figure 6 shows the blood flow velocity at different sections under 50% and 80% stenosis. The velocity distributions at sections S1–S4 are almost the same, which are

consistent with the distribution of the inlet velocity. At 0.23 s, the peak value at section S1 is more than 0.65 m/s, and the peak values at sections S2–S4 are between 0.4 and 0.45 m/s. However, in diastole, the velocities at sections S2 and S3 on the left and right pulmonary arteries are higher than those at sections S1 and S4. When the degree of stenosis is 50%, the velocity begins to decrease rapidly. The maximum velocity at section S6 in systole is higher than that at section S5. The peak value at section S6 (50%) is about 0.325 m/s, and that at section S5 (50%) is about 0.25 m/s. The opposite situation occurs in diastole, and the peak value is about 0.17 m/s. After 0.45 s, there is a gradual downward trend. However, when the degree of stenosis is 80%, the velocities at 0.15 s reach the peak rapidly, and the peaks at sections S5 (80%) and S6 (80%) are about 0.07 m/s. At 0.34 s, there are the second peaks, about 0.05 m/s. After that, the velocities gradually tend to be stable.

Figure 7 shows the velocity streamlines under different stenosis degrees. In contrast, the flow velocity is high at the throat of the stenosis. In diastole, the blood flow appears vortex, especially in the area of arterial bifurcation. In addition, the blood flow velocity at both ends of the stenosis is low.
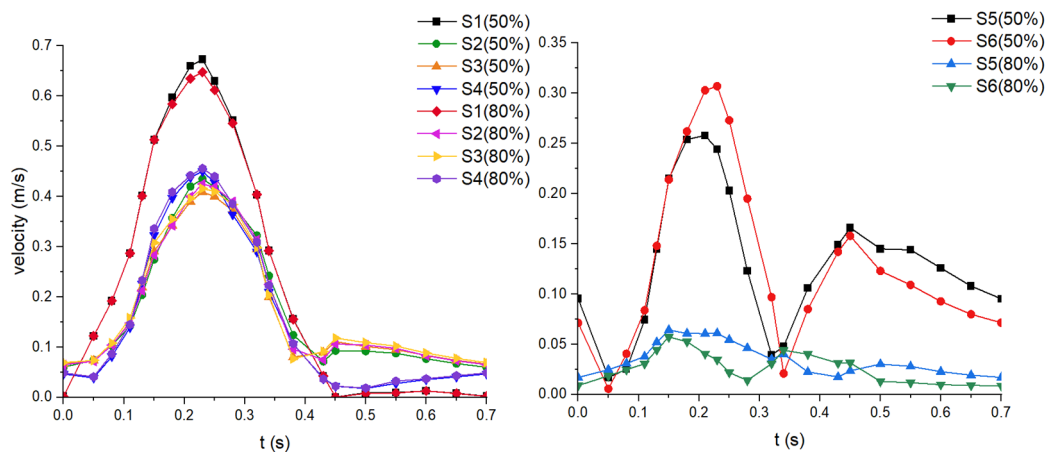

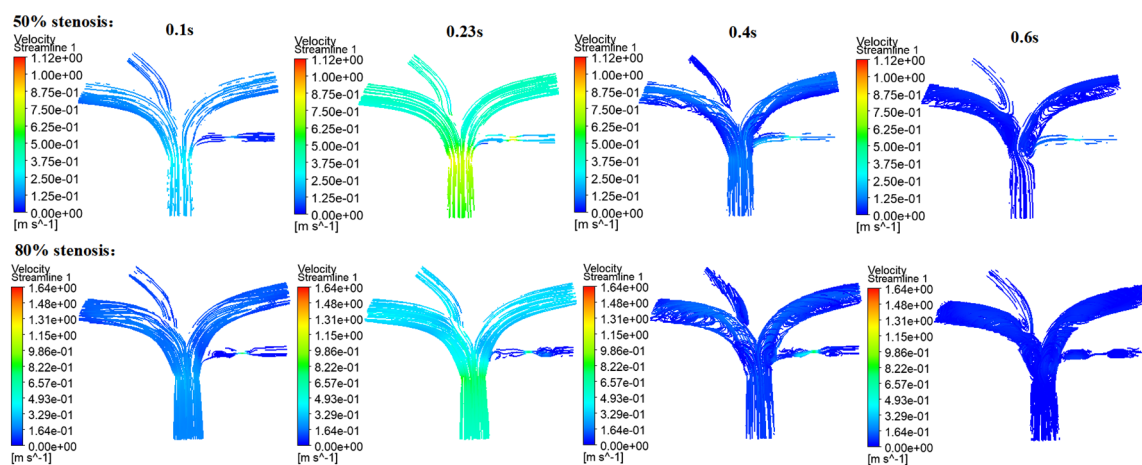**Figure 6.** Velocity distributions at different sections in two models.

Figure 7. Velocity streamlines at different moments in two models.

The wall shear stress distributions are described in Figure 8. When the degree of stenosis is 50%, the wall shear stresses at sections S5 and S6 reach the peaks at 0.23 s, about 1.2 and 0.8 Pa, respectively, and there are multiple peaks in cardiac diastole. Being similar to the blood flow velocity, when the degree of stenosis is 80%, the wall shear stresses at sections S5 and S6 reach the peaks at 0.15 and 0.34 s.
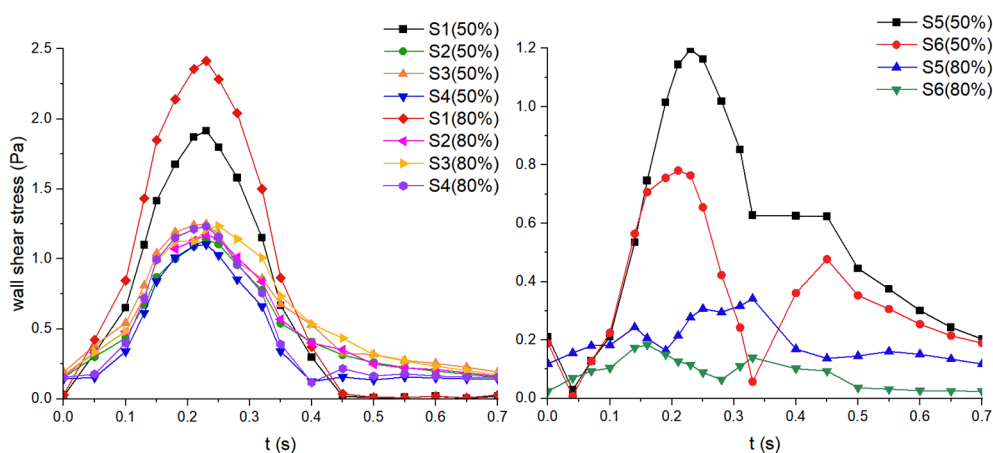

Figure 8. Wall shear stress distributions at different sections in two models.

4. Discussion

In order to more accurately and quantitatively analyze the influences of stenosis degree on QPPR and hemodynamics, only the stenosis degree in the two models is changed. The results are consistent with previous studies and clinical diagnosis results [23,24]. With the reference to the evaluation standard of FFR, we believe that when the stenosis degree is 80%, the patient's myocardial ischemia is serious, thus it may be necessary to conduct interventional treatment. When the stenosis degree is 50%, the treatment plan with drugs could be taken according to the actual situation of the patient. In addition, with the increase of stenosis degree, the blood flow resistance increases, resulting in a higher pressure drop. Hence, $\triangle P$ in Eq (3) is higher. According to Eqs (2) and (3), QPPR is inversely proportional to $\triangle P$, and thus QPPR decreases. Therefore, QPPR is closely related to $\triangle P$. The higher the pressure drop, the lower the QPPR. Furthermore, the QPPR value may be an indicator of stenosis degree.

Compared with pressure, blood flow velocity and wall shear stress are more sensitive to the degree of stenosis, especially at the branch of stenosis. From the numerical results, it is obvious that the variation trends of blood flow velocity and wall shear stress are related to the degree of stenosis. The velocity streamlines show that under the condition of arterial stenosis, low speed vortex occurs, the elasticity of blood vessels decreases and blood viscosity increases, which lead to insufficient blood supply to the human body. In addition, there is resistance reflection at both ends of the stenosis, resulting in peak superposition. Previous studies have found that wall shear stress could be used as an important marker for disease prediction [25]. Wall shear stress affects the normal physiological activity of endothelial cells. High or low wall shear stress indicates that pulmonary artery stenosis is developing along a negative direction. Therefore, the changes of hemodynamic parameters of pulmonary artery stenosis could be used as the important information for clinical diagnosis and treatment. Therefore, the

contributions of this work are to introduce the concept of QPPR, and determine the relationship between stenosis degree and QPPR. Similar to the coronary QFR, QPPR is noninvasive and could be obtained by numerical calculation. It may be very important for clinicians to quickly diagnose the patient's condition and give treatment plans. As is well known, when the coronary FFR is lower than 0.75, the ability of the coronary artery to supply blood is blocked, resulting in myocardial ischemia and requiring interventional procedures. When FFR is between 0.75 and 0.8, which belongs to the "grey zone", clinicians could select the appropriate treatment through the patient's current situation. When FFR is higher than 0.8, conservative treatment with drugs could be taken. Thus, according to similar criteria of FFR, QPPR may be used to determine therapy of pulmonary artery stenosis.

In this study, the construction of the idealized model of pulmonary artery stenosis deviates from the real shape. In the condition setting of hemodynamic simulation, Newtonian blood and the isotropic linear elastic model of arterial wall are adopted, ignoring the complexity of blood and arterial wall. According to arterial experimental data, the artery should be a hyperelastic and viscoelastic anisotripic material [26–28]. In addition, there are residual stresses in arteries. Residual stresses have an important influence on the aorta wall mechanics and, in particular, on the stress-strain distribution through the wall [29]. In a future study, three-dimensional reconstruction will be performed according to the stenosis branch of specific patients, which improves the accuracy of modeling, optimizes the stenosis model and makes it more similar to the real physiological environment. As for numerical simulations, SOFNN-HPS [30], GK-ARFNN [31] and AQPSO-SOFNN [32] methods could have higher predictions.

5. Conclusions

We focus on QPPR studies based on 50% and 80% stenosis. The results suggest that the degree of pulmonary artery stenosis has a significant impact on QPPR and hemodynamic changes. The QPPR value is closely related to the pressure drop. Blood flow velocity and wall shear stress are highly sensitive to the degree of stenosis. The QPPR in the 80% stenosis model is lower. This study lays a theoretical foundation for the further study of QPPR.

Use of AI tools declaration

The authors declare they have not used Artificial Intelligence (AI) tools in the creation of this article.

Acknowledgments

Conflict of interest

The authors declare that there are no conflicts of interest.

References

1. M. P. Wasserman, P. J. Varghese, R. D. Rowe, The evolution of pulmonary arterial stenosis associated with congenital rubella, *Am. Heart J.*, **76** (1968), 638–644. https://doi.org/10.1016/0002-8703(68)90162-2

2. N. H. Pijls, J. A. van Son, R. L. Kirkeeide, B. De Bruyne, K. L. Gould, Experimental basis of determining maximum coronary, myocardial, and collateral blood flow by pressure measurements for assessing functional stenosis severity before and after percutaneous transluminal coronary angioplasty, *Circulation*, **87** (1993), 1354–1367. https://doi.org/10.1161/01.CIR.87.4.1354

3. F. Díez-Delhoyo, E. Gutiérrez-Ibañes, F. Fernández-Avilés, Functional disorders in non-culprit coronary arteries and their implications in patients with acute myocardial infarction, *Trends Cardiovasc. Med.*, **30** (2020), 346–352. https://doi.org/10.1016/j.tcm.2019.08.011

4. G. Franchini, F. Giovanniello, M. Amabili, Viscoelasticity of human descending thoracic aorta in a mock circulatory loop, *J. Mech. Behav. Biomed. Mater.*, **130** (2022), 105205. https://doi.org/10.1016/j.jmbbm.2022.105205

5. N. Suzuki, S. Nishide, T. Kimura, T. Aoyagi, K. Kanamori, Y. Shiratori, et al., Relationship of quantitative flow ratio after second-generation drug-eluting stent implantation to clinical outcomes, *Heart Vessels*, **35** (2020), 743–749. https://doi.org/10.1007/s00380-019-01545-4

6. S. Tu, J. Westra, J. Yang, C. von Birgelen, A. Ferrara, M. Pellicano, et al., Diagnostic accuracy of fast computational approaches to derive fractional flow reserve from diagnostic coronary angiography: the international multicenter FAVOR pilot study, *JACC Cardiovasc. Interventions*, **9** (2016), 2024–2035. https://doi.org/10.1016/j.jcin.2016.07.013

7. T. Inami, M. Kataoka, N. Shimura, H. Ishiguro, R. Yanagisawa, K. Fukuda, et al., Pressure-wire-guided percutaneous transluminal pulmonary angioplasty: A breakthrough in catheter-interventional therapy for chronic thromboembolic pulmonary hypertension, *JACC Cardiovasc. Interventions*, **7** (2014), 1297–1306. https://doi.org/10.1016/j.jcin.2014.06.010

8. F. J. H. Gijsen, F. N. van de Vosse, J. D. Janssen, The influence of the non-Newtonian properties of blood on the fow inlarge arteries: Steady fow in a carotid bifurcation model, *J. Biomech.*, **32** (1999), 601–608. https://doi.org/10.1016/s0021-9290(99)00015-9

9. H. Yao, K. C. Ang, J. H. Yeo, E. K. Sim, Computational modelling of blood flow through curved stenosed arteries, *J. Med. Eng. Technol.*, **24** (2000), 163–168. https://doi.org/10.1080/03091900050163445

10. Z. Q. Wang, Y. J. Zhou, Y. X. Zhao, D. M. Shi, Y. Y. Liu, W. Liu, et al., Diagnostic accuracy of a deep learning approach to calculate FFR from coronary CT angiography, *J. Geriatr. Cardiol.*, **16** (2019), 42–48.

11. S. Molloi, Y. Zhou, G. S. Kassab, Regional volumetric coronary blood flow measurement by digital angiography: In vivo validation1, *Acad. Radiol.*, **11** (2004), 757–766. https://doi.org/10.1016/j.acra.2004.04.002

12. C. Abugattas, A. Aguirre, E. Castillo, M. Cruchaga, Numerical study of bifurcation blood flows using three different non-Newtonian constitutive models, *Appl. Math. Modell.*, **88** (2020), 529–549. https://doi.org/10.1016/j.apm.2020.06.066

13. F. Kong, V. Kheyfets, E. Finol, X. C. Cai, Simulation of unsteady blood flows in a patient-specific compliant pulmonary artery with a highly parallel monolithically coupled fluid-structure interaction algorithm, *Int. J. Numer. Method Biomed. Eng.*, **35** (2019), 1–25. https://doi.org/10.1002/cnm.3208

14. M. Jahangiri, M. Saghafian, M. R. Sadeghi, Numerical simulation of hemodynamic parameters of turbulent and pulsatile blood flow in flexible artery with single and double stenoses, *J. Mech. Sci. Technol.*, **29** (2015), 3549–3560. https://doi.org/10.1007/s12206-015-0752-3

15. J. P. O'Callaghan, E. R. Heitzman, J. W. Somogyi, B. A. Spirt, CT evaluation of pulmonary artery size, *J. Comput. Assisted Tomogr.*, **6** (1982), 101–104. https://doi.org/10.1097/00004728-198202000-00017

16. D. Tang, C. Yang, H. Walker, S. Kobayashi, D. N. Ku, Simulating cyclic artery compression using a 3D unsteady model with fluid–structure interactions, *Comput. Struct.*, **80** (2002), 1651–1665. https://doi.org/10.1016/S0045-7949(02)00111-6

17. K. L. Gould, Pressure-flow characteristics of coronary stenoses in unsedated dogs at rest and during coronary vasodilation, *Circ. Res.*, **43** (1978), 242–253. https://doi.org/10.1161/01.RES.43.2.242

18. P. Stradins, R. Lacis, I. Ozolanta, B. Purina, V. Ose, L. Feldmane, et al., Comparison of biomechanical and structural properties between human aortic and pulmonary valve, *Eur. J. Cardiothorac. Surg.*, **26** (2004), 634–639. https://doi.org/10.1016/j.ejcts.2004.05.043

19. T. J. Pedley, *The Fluid Mechanics of Large Blood Vessel*, Cambridge: Cambridge University Press, 1980. https://doi.org/10.1017/CBO9780511896996

20. N. Bessonov, A. Sequeira, S. Simakov, Y. Vassilevskii, V. Volpert, Methods of blood flow modelling, *Math. Modell. Nat. Phenom.*, **11** (2016), 1–25. https://doi.org/10.1051/mmnp/201611101

21. M. J. Chern, M. T. Wu, S. W. Her, Numerical study for blood flow in pulmonary arteries after repair of tetralogy of Fallot, *Comput. Math. Methods Med.*, **2012** (2012), 1–18. https://doi.org/10.1155/2012/198108

22. C. A. Taylor, J. D. Humphrey, Open problems in computational vascular biomechanics: Hemodynamics and arterial wall mechanics, *Comput. Methods Appl. Mech. Eng.*, **198** (2009), 3514–3523. https://doi.org/10.1016/j.cma.2009.02.004

23. H. Xu, J. Liu, D. Zhou, Y. Jin, Influence of microcirculation load on FFR in coronary artery stenosis model, *BMC Cardiovasc. Disord.*, **20** (2020), 1–7. https://doi.org/10.1186/s12872-020-01437-w

24. S. Kamangar, I. A. Badruddin, K. Govindaraju, N. Nik-Ghazali, A. Badarudin, G. N. Viswanathan, et al., Patient-specific 3D hemodynamics modelling of left coronary artery under hyperemic conditions, *Med. Biol. Eng. Comput.*, **55** (2017), 1451–1461. https://doi.org/10.1007/s11517-016-1604-8

25. J. Zhou, Y. S. Li, S. Chien, Shear stress-initiated signaling and its regulation of endothelial function, *Arterioscler., Thromb., Vasc. Biol.*, **34** (2014), 2191–2198. https://doi.org/10.1161/ATVBAHA.114.303422

26. G. Franchini, I. D. Breslavsky, G. A. Holzapfel, M. Amabili, Viscoelastic characterization of human descending thoracic aortas under cyclic load, *Acta Biomater.*, **130** (2021), 291–307. https://doi.org/10.1016/j.actbio.2021.05.025

27. M. Amabili, M. Asgari, I. D. Breslavsky, G. Franchini, F. Giovanniello, G. A. Holzapfel, Microstructural and mechanical characterization of the layers of human descending thoracic aortas, *Acta Biomater.*, **134** (2021), 401–421. https://doi.org/10.1016/j.actbio.2021.07.036

28. M. Amabili, P. Balasubramanian, I. Bozzo, I. D. Breslavsky, G. Ferrari, Layer-specific hyperelastic and viscoelastic characterization of human descending thoracic aortas, *J. Mech. Behav. Biomed. Mater*., **99** (2019), 27–46. https://doi.org/10.1016/j.jmbbm.2019.07.008

29. I. D. Breslavsky, M. Amabili, Nonlinear model of human descending thoracic aortic segments with residual stresses, *Biomech. Model. Mechanobiol.*, **17** (2018), 1839–1855. https://doi.org/10.1007/s10237-018-1060-5

30. H. Zhou, Y. Zhang, W. Duan, H. Zhao, Nonlinear systems modelling based on self-organizing fuzzy neural network with hierarchical pruning scheme, *Appl. Soft. Comput*., **95** (2020), 106516. https://doi.org/10.1016/j.asoc.2020.106516

31. H. Zhou, Y. Li, Q. Zhang, H. Xu, Y. Su, Soft-sensing of effluent total phosphorus using adaptive recurrent fuzzy neural network with Gustafson-Kessel clustering, *Expert Syst. Appl*., **203** (2022), 117589. https://doi.org/10.1016/j.eswa.2022.117589

32. H. Zhou, Y. Li, H. Xu, Y. Su, L. Chen, A self-organizing fuzzy neural network modeling approach using an adaptive quantum particle swarm optimization, *Appl. Intell*., **53** (2023), 13569–13592. https://doi.org/10.1007/s10489-022-04133-8